Carboxylic acid-capped ruthenium nanoparticles: experimental and theoretical case study with ethanoic acid

Roberto Gonzalez-Gomez, Lucy Cusinato, Christian Bijani, Yannick Coppel, Pierre Lecante, Catherine Amiens, Iker Del rosal, Karine Philippot, Romuald Poteau

Carboxylic acid-capped ruthenium nanoparticles: experimental and theoretical case study with ethanoic acid[†]

González-Gómez, Roberto[(a,b)]; Cusinato, Lucy[(a)]; Bijani, Christian[(b)]; Coppel, Yannick[(b)]; Lecante, Pierre[(c)]; Amiens, Catherine[(b)]; del Rosal, Iker[(a)]; Philippot, Karine[*(b)]; Poteau, Romuald[*(a)]
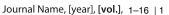
Given the properties of metal nanoparticles (NPs) depend on several parameters (namely, morphology, size, surface composition, crystalline structure, etc.) a computational model that brings a better understanding of structure/properties relationship at the nanoscale is a significant plus in order to explain the surface properties of metal NPs and also their catalytic viability, in particular when envisaging a new stabilizing agent. In this study we combined experimental and theoretical tools to obtain a mapping of the surface of ruthenium NPs stabilized by ethanoic acid as a new capping ligand. For that purpose, the organometallic approach was applied as synthesis method. The morphology and crystalline structure of the obtained particles was characterized by state-of-the art techniques (TEM, HRTEM, WAXS) and their surface composition was determined by various techniques (solution and solid-state NMR, IR, chemical titration, DFT calculations). DFT calculations of the vibrational features of model NPs and of the chemical shifts of model clusters allowed to secure the spectroscopic experimental assignations. Spectroscopic data as well as DFT mechanistic studies showed that the ethanoic acid lies on the metal surface as ethanoate, together with hydrogen atoms. The optimal surface composition determined by DFT calculations appeared to be *ca.* [0.4-0.6] H/Ru_{Surf} and 0.4 ethanoate/Ru_{Surf}, which was corroborated by experimental results. Moreover, for such a composition, an hydrogen adsorption Gibbs free energy in the range -2.0 to -3.0 kcal.mol^{-1} was calculated, which makes these ruthenium NPs a promising nanocatalyst for the hydrogen evolution reaction in the electrolysis of water.

1 Introduction

The interest in metal nanoparticles (NPs) continues to be very strong in both the academic and industrial sectors owing to their possible applications in various fields ranging from biology, medicine, catalysis, optoelectronics, to energy.[1–5] This interest is prompted by the specific properties displayed by metal NPs, usually different to those of matter and molecular transition metal complexes or small clusters. This relies on an electronic structure intermediate between the quantized levels in finite-size small compounds and the band structure in solids. It depends on the shape of the metal core, its size, the possible presence of defects and the nature and surface coverage of capping ligands. Given their specific properties, metal NPs are nowadays proposed and investigated as multipurpose species for innovative applications. There is thus a need to produce them in a reproducible and controlled manner in terms of size, shape and composition. The organometallic approach is a powerful way to meet this target. It involves coordination chemistry, from the use of metal complexes as metal sources, of ligands as stabilizing agents, and of additional chemical species to decompose and in some cases to reduce the complexes, as well as intricated and complex thermodynamic and kinetic parameters during the growth process. When metal NPs are stabilized with covalently bound ligands,

[a] LPCNO (IRSAMC), Université de Toulouse; INSA, UPS, CNRS (UMR 5215); Institut National des Sciences Appliquées, 135 avenue de Rangueil, F-31077 Toulouse, France; E-mail: romuald.poteau@univ-tlse3.fr

[b] LCC-CNRS, Université de Toulouse, UPS, 205 route de Narbonne, BP 44099, F-31077-Toulouse Cedex 4, France; E-mail: karine.philippot@lcc-toulouse.fr

[c] CEMES-CNRS, 29 rue Jeanne Marvig BP4347, 31055 Toulouse Cedex, France.

† Electronic Supplementary Information (ESI) available: TEM images and corresponding size histogram of $Ru_x(CH_3COOH)_{0.2}$ NPs; WAXS diagram and RDF profile of $Ru_x(CH_3COOH)_{0.4y}$ NP; Experimental ^1H-NMR spectrum of $Ru_x(CH_3COOH)_{0.4y}$ NPs compared with DFT NMR data; basis set effect on the ^1H and ^{13}C DFT-NMR chemical shifts of ethanoic acid and ethanoate in different models; surface composition, energies, labeling and coordination of the surface species in the 44 models used within the *ab initio* thermodynamics method; geometries provided as cartesian coordinates (in Å); energies given in eV. See DOI: 10.1039/b000000x/

their surface composition is a key factor that influences the electronic structure of the metal core. The size and charge of surface ligands can also tune the inter-particle interaction, and induce different self-assembly properties. A suitable choice of metal precursors (and consequently of the by-products issued from the synthesis) and of functionalizing surface species will also directly act on the metal NPs solubility. Despite the fascinating diversity of metal NPs already produced, it is still necessary to modify their surface in a controlled manner in order to improve their properties and extend their multifunctionality. Regarding ruthenium NPs, they have been reported to be stabilized by amines, phosphines, pyridines, carbenes, alcohols, betaines, carbon monoxide...[6–9] Yet, although carboxylic acids are widely used as surfactants in colloids synthesis (mainly in combination with amines), to our knowledge there is only one reported attempt to stabilize small ruthenium NPs with carboxylic acids, namely with hexasubstituted fullerene $C_{66}(COOH)_{12}$.[10] From a more general point of view, whilst adsorption of formic acid on metal surfaces is a long-standing case study,[11] both because of fundamental issues[12] and because it is identified as an hydrogen source,[13] adsorption of carboxylic acids RCOOH (R≠H) on metal surfaces have received less attention.
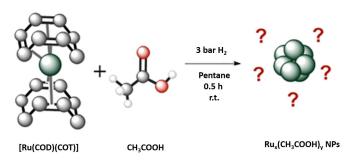
Here, we present a study where computational and experimental chemistry team up and complement one another, in order to fully characterize CH_3COOH-functionalized ruthenium NPs and to provide insights on their electronic structure. This joint strategy provides new clues to experimentalists about the 3D representation of small metal NPs, their surface chemistry and the balance between surface coverage and adsorption energies. According to the Brønsted-Evans-Polanyi (BEP) relationship,[14,15] and to the Sabatier-Balandin concepts,[16] assessing actual adsorption energies is an important prerequisite to understand the catalytic properties of metal NPs. From a computational chemistry point of view, it is necessary to explore the physical or chemical properties of a chemical system on a structural 3D model, including surface species, that must be as close as possible to the experimental compound and that must be within the reach of first principles method. This is a challenging goal regarding organometallic metal NPs.

We show here that it is possible to bring computational chemistry applied to small nanoparticles to the same level of accuracy and relevance as in molecular chemistry. We thus report the synthesis of ruthenium NPs stabilized with ethanoic acid and their characterization by transmission electron microscopy (TEM), ^1H and ^{13}C nuclear magnetic resonance (NMR) and infrared (IR) spectroscopy. The spectroscopic experimental assignations are secured with DFT calculations of the vibrational features of model NPs as well as with the chemical shifts in model clusters. The surface chemistry of these new CH_3COOH-functionalized ruthenium NPs is also investigated and discussed both experimentally and theoretically, including calculations of atomic charges and d-band centers. The possibility to use such NPs in the context of the hydrogen evolution reaction (HER) is also evaluated on the basis of DFT calculations and of the Sabatier-Balandin principle.[17] The results highlight the relationship between surface composition and dissociative adsorption energies of H_2. It further strengthens the

need to carefully evaluate the surface composition of model NPs, in order to make theoretical investigations in this field useful and relevant.

2 Results

2.1 Synthesis and structural characterization of CH_3COOH-functionalized ruthenium NPs

The NPs object of this study were produced in a Fisher-Porter reactor at room temperature (r.t.) by the decomposition of [Ru(COD)(COT)] (COD= 1,5 cyclooctadiene, COT= 1,3,5- cyclooctatriene) with molecular hydrogen (H_2) in a pentane solution and in the presence of ethanoic acid (CH_3COOH) as a stabilizer (Scheme 1).

Scheme 1 Synthesis of CH_3COOH-capped rutheniumNPs.

A [CH_3COOH]/[Ru] ratio of 0.2 molar equivalent (equiv.) compared to the quantity of the Ru precursor introduced was first applied. This [CH_3COOH]/[Ru] ratio was chosen because it is known to be effective to prepare stable and homogeneous populations of ruthenium NPs using different capping ligands.[7,18] After pressurization of the Fisher Porter reactor with 3 bar H_2 under vigorous stirring at r.t., the initial yellow solution turned black into *ca.* 2 min. The hydrogen pressure was maintained at r.t. during 30 min to ensure complete decomposition of the [Ru(COD)(COT)] precursor, meanwhile some precipitation was observed. Then, excess H_2 was evacuated under vacuum and the colloidal suspension concentrated by half. Transmission Electron Microscopy (TEM) images recorded after deposition of a drop of the crude concentrated colloidal suspension onto a carbon-covered copper grid, revealed a non-homogeneous sample (Figure SI.1): two different populations of individual ruthenium NPs were observed with mean diameters of *ca.* 0.8 and 1.2 nm, together with agglomerated particles in the size range 50-180 nm. The presence of these big agglomerates can explain the formation of the precipitate noticed during the synthesis. Given small ruthenium NPs were observed, we estimated that the ethanoic acid was able to act as a stabilizer and that the inhomogeneity of the sample could be attributed to a default of the capping ligand quantity. The synthesis of the particles was thus repeated in the same conditions increasing the [CH_3COOH]/[Ru] ratio to 0.4 equiv. By this way, no precipitate was observed over the course of the reaction (30 min), but the NPs slowly sedimented when stopping the magnetic stirring for a few hours. This phenomenon can derive from a limited solubility of the NPs in pentane due to the short aliphatic tail and strongly polar head of the ethanoic

acid ligand. TEM analysis from the crude concentrated colloidal suspension evidenced NPs with a mean size of *ca.* 1.5 ± 0.6 nm (Figure 1b) and a spheroid morphology forming a population with a relatively large size distribution, but no aggregates were observed this time (Figure 1a). The increase of the ethanoic acid quantity to 0.4 equiv. [CH₃COOH]/[Ru] leading thus to NPs of enhanced stability in solution we decided to focus on this $Ru_x(CH_3COOH)_{0.4y}$ system for the rest of our experimental study. HRTEM (high resolution transmission electron microscopy) analysis (Figure 1c and Figure SI.2) showed NPs displaying a poor crystalline character but with a few atomic plans sufficiently visible to resolve the crystal structure of some NPs. Fast Fourier Transformation (FFT) of HRTEM images indicated the presence of interplanar distances of 0.238 and 0.208 nm that can be attributed to (100) and (101) lattice planes of an hexagonal close packed (hcp) structure as in bulk ruthenium. Moreover, energy-dispersive X-ray spectroscopy (EDX) data recorded in parallel of HRTEM analysis allowed to quantify Ru and O contents. The obtained values led to a Ligand/Ru_{surf} ratio of *ca.* 0.27 (see Figure SI.3 and Table SI.4).

WAXS analysis for solid-state $Ru_x(CH_3COOH)_{0.4y}$ was performed to complete the local study by TEM with a statistic probe. Such approach has been routinely used for previous studies and with few exceptions, both structure and average size (through the coherence length measured in real space) were in good agreement, provided the NPs were close to single crystals, even very small. This is not fully verified in the present case: in the reciprocal space (Figure SI.5), a very broad pattern is observed which doesn't match those expected from compact structures. Moreover, in the real space (Figure SI.6), a well-defined function fully consistent with zerovalent metallic ruthenium can be observed. However the coherence length is close to 0.9 nm, thus considerably smaller than the size obtained by TEM. The function computed from a very small hcp crystallite also does not fit the experimental one. This is not in contradiction with TEM results since WAXS is sensitive to very small objects, crystalline or not, whilst HRTEM largely relies on phase contrast and emphasizes the better crystallized fraction of a sample. This result is likely a consequence of the relatively large size distribution: in such a case, WAXS will evidence the contribution of many very small and poorly crystallized objects, the hcp NPs revealed by HRTEM being related to bigger and better ordered domains. This dual population from the size and structure point of view may indicate a limited coalescence of the very small ruthenium NPs leading to bigger domains.[19]

Two complementary spectroscopic techniques, namely nuclear magnetic resonance (NMR; both in liquid and solid state as well as DOSY experiments) and IR were used to analyze the coordination of the ethanoic acid to the NP surface and thus, to characterize the surface state of the $Ru_x(CH_3COOH)_{0.4y}$ NPs. The results will be presented in forthcoming sections, together with DFT-based analysis, when available. Our main objective was to get information about the surface composition of the $Ru_x(CH_3COOH)_{0.4y}$ NPs and the nature of the bonding of the stabilizing ligands.

2.2 Are ethanoic acid ligands adsorbed on the NPs?

NMR techniques coupled with theoretical calculations provided relevant information to answer this question. It is worth noting that obtaining reliable information on ligands coordinated at the surface of NPs by solution NMR analysis is not a simple task. This is mainly due to the low concentration of coordinated ligands compared to metal atoms in the NP core, the diversity of coordination sites at the metal surface, the heterogeneity of the magnetic environment of the atoms in the ligand owing to the decrease of its freedom degrees and slow tumbling of the NPs. All together these parameters lead to broad and weak signals that are sometimes very difficult to observe all the more so when the probe atoms are close to the metal surface, as it is the case here with ethanoic acid. Furthermore, short alkyl chain ligands do not help the solubilization of the NPs thus leading to a weak NP concentration in the colloidal suspension. Nevertheless, a combination of complementary NMR tools allowed to get relevant information on the ligands attached at the ruthenium surface which was corroborated by theoretical approach. ^{1}H-NMR studies are described hereafter.

A proton-liquid NMR (^{1}H-NMR) spectrum was recorded from the purified $Ru_x(CH_3COOH)_{0.4y}$ NPs (washing of the crude sample with several pentane-THF cycles and drying under vacuum during 12 h) after re-dispersion in THF-d^8. This ^{1}H-NMR spectrum is given in Figure SI.7 in comparison with that of pure ethanoic acid as a reference for the free (uncoordinated) acid. Apart from the signals at 3.62 and 1.76 ppm that correspond to THF and the one at 2.55 ppm that can be attributed to water, the spectrum of the NPs (Figure SI.7, solid green line) does not show any sharp signals around 1.93 and 10.59 ppm as expected for free CH_3COOH (Figure SI.7, dash burgundy line). This result suggests that the THF-d^8 solution of $Ru_x(CH_3COOH)_{0.4y}$ NPdoes not contain free ethanoic acid. However, broad and sharp singlets are visible in the 1.90 to 2.20 ppm range that might correspond to methyl groups of ethanoic acid molecules in fast exchange between the surface of the NPs and the solution. Besides, several sharp peaks of low intensity can be observed in different area of the spectrum that may derive from THF degradation. This point will be discussed later on.

Pulse field gradient NMR technique can be used as a diffusion-filtered ^{1}H-NMR experiment to reduce the contribution of mobile molecules with fast diffusion coefficients like free ligands, side products or solvents, thereby giving the possibility to observe signals corresponding to larger species with lower diffusion coefficients such as ligands interacting with the NP surface. This methodology has been already applied in the group and allowed to distinguish signals of free ligands in solution from those of ligands interacting at a metal NP surface. [20–22] The application of a diffusion-filter to the $Ru_x(CH_3COOH)_{0.4y}$ NPs solution, allowed to detect a new broad signal that is characteristic of slow diffusing species at *ca.* 2.08 ppm (FWHM = 1150 Hz, Figure 2). This value is close to the chemical shift observed for the methyl group protons of the ethanoic acid (δ: 1.93 ppm). Due to its position and broadness, as well as to previous surface state studies on ligand-capped ruthenium NPs, this slightly shifted signal in comparison
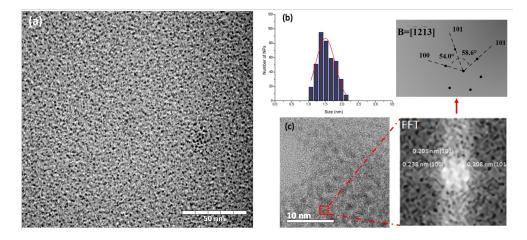
Fig. 1 TEM image and corresponding size histogram of $Ru_x(CH_3COOH)_{0.4y}$ NPs (a, b); HRTEM image of $Ru_x(CH_3COOH)_{0.4y}$ NPs with FFT results (c).

to that of free CH_3COOH can be attributed to the methyl group protons of ethanoic acid strongly bonded to the ruthenium NPs surface.
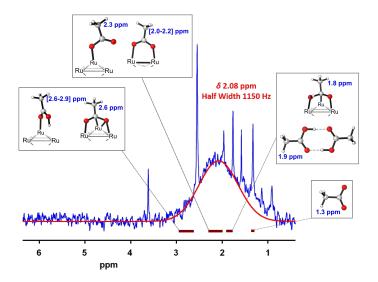

Fig. 2 Diffusion-filtered ^1H NMR spectrum of $Ru_x(CH_3COOH)_{0.4y}$ NPs dispersed in THF-d^8 at r.t. The broad signal at *ca.* 2.08 ppm was fitted with a Gaussian shape. The DFT ^1H NMR chemical shifts of the methyl group in various models (($CH_3COOH)_2$, CH_3COO^-, $[Ru_6]$ clusters) are also given. The DFT results are summarized by the burgundy horizontal lines.

This assignment is confirmed by DFT chemical shifts calculated for protonated/unprotonated carboxylic acid free and coordinated onto a model $[Ru_6]$ cluster (see Figure 2 and Table SI.8), the molecular cluster strategy for such NMR calculations having been validated by us [23–27] and others. [28] The protons of the methyl group of free ethanoic acid dimer are found to resonate at 1.9 ppm as experimentally observed (1.93 ppm). The protons of the methyl group in all the $Ru_6(CO)_n(CH_3COOH)$ clusters were found to be strongly deshielded by the metal surface (δ: [2.6 - 2.9] ppm). This strong deshielding effect is confirmed by calculations performed on small molecules (see Table SI.8) which rules out this coordination mode in the NPs studied here. Thus, accord-

ing to our results, there is no doubt that the signal experimentally observed at *ca.* 2.08 ppm cannot be assigned to ethanoic acids coordinated on the metal surface but to chemisorbed ethanoates (δ: [2.0 - 2.3] ppm). Indeed, the signal of the protons of the methyl group is deshielded by *ca.* 0.1 ppm for an ethanoate coordinated on an edge via a bidentate mode. The three methyl protons in the free ethanoate are shielded by 0.6 ppm with respect to those of the free ethanoic acid dimer by the delocalized negative charge of the carboxylate group (δ: 1.3 ppm vs. 1.9 ppm). The interaction of the -COO- negative moiety with a metal cation in sodium ethanoate weakens the shielding of the methyl protons by the negative charge by 0.6 ppm (δ: 1.9 ppm, close to the value found in D_2O [29]). As a result of this counterbalance, the methyl protons in a metal-ethanoate complex resonate at a value close to those of ethanoic acid, with a modulation of the deshielding which is function of the cationic charge of the metal atom (for example, δ is found to be 2.1 ppm in the $(CH_3COO^-)_2Mg^{2+}$ complex).

Diffusion-Ordered NMR Spectroscopy (DOSY-NMR) also allows to get information on the dynamic behaviour of chemical compounds dispersed into a liquid environment. Here (*i.e.* on $Ru_x(CH_3COOH)_{0.4y}$ NPs dispersed in THF-d^8 at r.t.) the strong overlapping between the broad signal of low intensity attributed to the methyl groups of the surface attached ligand with the sharp signals of fast exchanging molecules, makes the DOSY data difficult to analyse. However, interesting information were obtained by following the evolution of the integration of the 1.90 - 2.20 ppm area - that mostly presents signals of the methyl groups of ethanoates in interaction with the ruthenium NP surface - with the gradient strength. This diffusional attenuation is shown on Figure 3 and was fitted to the classical Stejskal-Tanner equation. The decay could not be fitted with a mono-exponential analysis and only a bi-exponential analysis least-square fitting led to a perfect match of the experimental data.
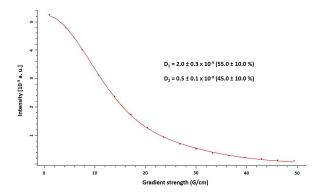
Fig. 3 Diffusional attenuation of the 1.90 - 2.20 ppm area for $Ru_x(CH_3COOH)_{0.4y}$ NPs dispersed in THF-d^8 at r.t. Data were analysed with a bi-exponential least-square fitting.

Two different diffusion coefficients (D) were extracted from this fitting, one representing 55.0 ± 10.0 % of the signal with $D_1 = 2.0 ± 0.3 × 10^{-9}$ m^2.s^{-1} and the other one representing 45.0 ± 10.0 % of the signal with $D_2 = 0.5 ± 0.1 × 10^{-9}$ m^2.s^{-1}. The significant difference between the two diffusion coefficients obtained is indicative of capping ligands with different interaction strengths at the NP surface, namely a distinction between coordinated ligands and fast exchanging molecules. The lower diffusion coefficient is attributed to ligands in strong interaction with the metal surface (namely, strongly coordinated ligands) and the faster one is assigned to ligands with higher mobility that can be in fast exchange with free ligand in solution or possible THF degradation products. The population of the strongly bonded species (45.0 ± 10.0 %) must be considered as a minimal value. Indeed, as a significant part of the very broad signal of the slow diffusing species detected at ca. 2.08 ppm lies outside the 2.20 - 1.90 ppm range, the population of strongly bonded ligands is probably much higher. Hydrodynamic radii (r_H) calculated from the diffusion coefficients (familiar Stokes-Einstein equation) were found to be ca. 0.94 and 0.24 nm, respectively. From these results, the size of the objects having the smallest diffusion coefficient can be estimated to 1.88 nm, including both the metal core and the capping-ligand layer. When comparing this value with the NPs mean diameter determined from TEM analysis (ca. 1.50 nm), that represents only the metal core, a good agreement is observed. The difference between these two values (0.38 nm) can be explained by the thickness of the layer of ligands surrounding the metal core. The hydrodynamic radius calculated for the species having the highest diffusion coefficient provided an estimated size for the corresponding objects of 0.48 nm. This value being slightly larger than the one calculated for the free ethanoic acid dimer ($D = 2.1 × 10^{-9}$ m^2.s^{-1}, r_H = 0.22 nm), it confirms the presence of ligands in fast exchange between the surface and the solution. On the basis of the DOSY NMR data and the mean size of the particles determined by TEM, we could estimate the ligand quantity at the RuNP surface to be ca. 0.3 ligand / Ru$_{surf}$.

2.3 Are the adsorbed acids protonated?

A first indication of the deprotonation of the acid was obtained by ^{1}H NMR (see above). A full answer to this question will now be given on the basis of DFT-based thermodynamic and kinetic data, complementary to experimental NMR and IR results.

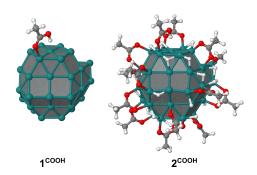**Adsorption strengths and O-H activation barrier: a theoretical survey.**

Fig. 4 $Ru_{55}(CH_3COOH)$, denoted as **1^{COOH}**, and $Ru_{55}(CH_3COOH)(CH_3COO)_{15}H_{32}$, denoted as **2^{COOH}**, models (15 hydrides result from COO-H activation in **2^{COOH}**). The faceting of the surface is highlighted with translucent gray planes.

As far as we know, there is no DFT study trying to answer that question on ruthenium surfaces, with the noticeable exception of formic acid. Previous DFT calculations showed that the O-H dissociation of HCOOH on a bare Ru(0001) surface is one of the most exothermic reaction among several model transition metal surfaces (-40 kcal.mol^{-1} w.r.t. gas-phase HCOOH).[30] Considering both the present experimental study as well as some spectroscopic and DFT evidences reported in Ref. 10, carboxylic acids seem to interact under the form of carboxylates with the ruthenium NPs surface. Before studying the optimal surface coverage by means of the first-principle thermodynamics, we will first consider the adsorption, kinetic and geometric properties of a single ethanoic acid on two hcp models which diameters are close to the WAXS coherence length of the experimental NPs: a bare 1 nm Ru$_{55}$ NP (model **1**, see section Methods) and the same Ru$_{55}$ NP, now stabilized by 15 ethanoates and 32 hydrides (model **2**). Model **2** provides reference data for the upper limit in terms of surface coverage (*vide infra*), model **1** being a lower limit with no surface species. The resulting species of the adsorption will later on be named **1^{COOH}** and **2^{COOH}**, see Figure 4. The ethanoic acid molecule is adsorbed on the same site in **1^{COOH}** and **2^{COOH}**, *i.e.* an edge between the (001) and (101) planes. Among the 32 hydrides present in **2^{COOH}**, 15 are considered to originate from the acid deprotonation. The metal surface thus accommodates 0.4 acids or carboxylates per surface Ru atom (Ru$_{surf}$) and 0.7 H/Ru$_{surf}$, a surface composition close to that of the Ru$_x(CH_3COOH)_{0.4y}$ experimental NPs, but with an hydride coverage slightly beyond the experimental evidence (*vide infra*).

With an adsorption energy of -23.9 kcal.mol^{-1} on the bare NP, to be compared for example to the adsorption energy of CO on the same model (∼ -45 kcal.mol^{-1}) ethanoic acid can be considered as moderately chemisorbed. It is even more weakly adsorbed on the surface of **2**, with an adsorption energy of -14.0 kcal.mol^{-1}, a value very similar to the dissociative adsorption energy of H$_2$
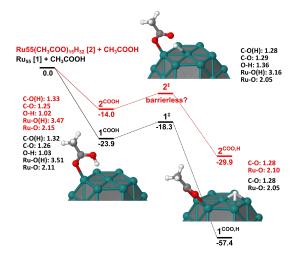
Ru55(CH₃COO)₁₅H₃₂ [2] + CH₃COOH
Ru₅₅ [1] + CH₃COOH

C-O(H): 1.28
C-O: 1.29
O-H: 1.36
Ru-O(H): 3.16
Ru-O: 2.05

0.0

2‡ barrierless?

C-O(H): 1.33
C-O: 1.25
O-H: 1.02
Ru-O(H): 3.47
Ru-O: 2.15

2**COOH**
-14.0

1‡
-18.3

1**COOH**
-23.9

C-O(H): 1.32
C-O: 1.26
O-H: 1.03
Ru-O(H): 3.51
Ru-O: 2.11

2**COO,H**
-29.9

C-O: 1.28
Ru-O: 2.10
C-O: 1.28
Ru-O: 2.05

1**COO,H**
-57.4

Fig. 5 Energy profile of the O-H bond dissociation. Black profile and energies: O-H activation on the bare Ru₅₅ NP (model **1**); red profile and energies: O-H activation on the Ru₅₅(CH₃COO)₁₅H₃₂ NP (model **2**). For the sake of clarity, geometries are shown for the bare case only; very similar geometries are found in model **2**. Energies are given in kcal.mol⁻¹. Some characteristic bond lengths are also given, in Å (same color convention as the energy profiles).

on bare Ru surfaces.[31] Although no steric hindrance impedes the grafting of an ethanoic acid, the presence of hydrides and ethanoates in the vicinity of the grafting site weakens its adsorption strength on the metal surface by lowering its d-band center (*vide infra*).[32,33]

Unsurprisingly, CH_3COOH dissociates very easily in **1**^{COOH}, to form an hydride adsorbed on the nearest edge and a carboxylate group (**1**^{COO,H}, see Figure 5, black profile), with a very small activation barrier of 5.6 kcal.mol⁻¹ (**1**‡). The resulting Ru₅₅(CH₃COO)(H) nanoparticle is more stable than the carboxylic acid counterpart by 33.5 kcal.mol⁻¹. The O-H bond dissociation energy (on the order of 112 kcal.mol⁻¹) is easily overcompensated by the hydrogen adsorption and the formation of a five-membered dimetallacycle involving the CH_3COO moiety. Some characteristic bond lengths are also given in Figure 5. On-going from the carboxylic acid group to its carboxylate counterpart, the Ru-O bond lengths are reduced by ∼0.06 Å, whereas the two C-O bonds have the same length, only 0.04 Å larger than a typical C=O bond length, indicating a conjugation within this dimetallacycle. Despite our efforts, no TS state has been found for **2**^{COOH}, which suggests an almost barrierless O-H activation, *i.e.* a very flat energy surface, on carboxylate-stabilized ruthenium NPs (**2**‡). Similarly to the bare case, the carboxylate/hydride species is thermodynamically more stable than the adsorbed carboxylic group (15.9 kcal.mol⁻¹). The grafting of this additional group is less favorable than on bare NPs. It is also interesting to evaluate the average dissociative adsorption energy of 16 ethanoic acids, *i.e.* the energy yield per ethanoic acid unit of the reaction Ru₅₅H₁₇ + 16CH₃COOH ⟶ **2**^{COO,H}, which is -35.1 kcal.mol⁻¹. It is close to the -29.9 kcal.mol⁻¹ energy calculated for the dissociative adsorption energy of CH_3COOH on model **2** (see Figure 5, red profile). It highlights the collective effect involved by the simultaneous adsorption of all ethanoic acids that makes the ad-

sorption of new ethanoates on the surface less and less exothermic. It must be mentioned at this point that an attempt to perform a geometry optimization of the Ru₅₅(CH₃COOH)₁₆H₁₇ compound, *i.e.* the carboxylic acid counterpart of **2**^{COOH}, led to a spontaneous decoordination of five acids from the metal surface. Given these thermodynamic and kinetic data, it can be assessed that carboxylic acids will readily form mainly carboxylate species on the surface, whatever its surface composition in the range [0 H, 0 EtAc - 0.7 H, 0.4 EtAc]/Ru$_{surf}$ - and probably beyond.

¹³C NMR experiments. As previously mentioned, heterogeneity, solubility and motion reduction (associated to dipolar couplings and chemical anisotropy) are some of the variables that can cause broad and weak signals in liquid NMR instead of sharp ones. The information obtained from solution NMR is thus very often not enough satisfying for determining the molecular structure or the intermolecular packing of ligands at NP surface.[34] In particular, the atoms the closest to the NP surface and even more importantly those directly attached, cannot be identified by liquid-state NMR. In this case, solid-state NMR can be an interesting alternative to reach information on the ligand shell. Indeed, application of a high-speed rotation at the magic angle (MAS) allows to reduce the dipolar interactions and anisotropy of the samples, thus leading to visible signals in solid-state NMR that are not accessible by solution NMR.

Previous works from the group proved solid-state NMR to be a powerful tool to get information on the ligand atoms close to the metal surface. For instance, ¹³C and ³¹P solid-state NMR allowed to get precise information on carbon and phosphorous atoms directly attached to the surface of ruthenium NPs stabilized by carbenes[35] or phosphines.[20,21] Given that, solid-state ¹³C CP Hahn-MAS NMR was attempted on the Ru$_x$(CH₃COOH)$_{0.4y}$ NPs in order to go more deeply into the characterization of their surface state. To avoid the formation of electric arcs between the NMR coils and the rotor due to the high metal content of the purified ruthenium NPs powder, the sample was dispersed by impregnation of mesoporous silica with a THF colloidal suspension of the NPs. The obtained data are presented in Figure 6 as well as results from DFT calculations for different coordination modes which have been used to assign the signals from the experimental spectrum.

The two intense peaks observed at *ca*. 24.2 and 66.8 ppm correspond to carbon atoms from residual THF. The broadness observed in the foot of the *ca*. 24.2 ppm signal may be attributed to the carbon of the methyl group of the ligand, as confirmed by the DFT-NMR calculations which show a weak dependence of this resonance for the protonation/deprotonation of the carboxylic group or to its coordination mode (20 ppm to 33 ppm according to the model). The broad signal observed above 170.0 ppm is in the expected area for carbon atoms of carboxylic groups from free CH_3COOH. The signal at *ca*. 186.0 ppm is downfield shifted compared with the signal of the C atom of the carboxyl group of this free CH_3COOH in THF-d^8 (171.7 ppm), an experimental value that is well reproduced by the DFT calculations obtained for the free CH_3COOH (172 ppm). But this DFT values could be shifted by taking into account solvent effects or by increas-
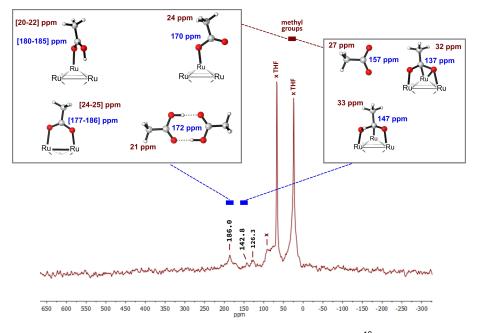
Fig. 6 ^{13}C CP Hahn-MAS NMR of $Ru_x(CH_3COOH)_{0.4y}$ NPs dispersed in mesoporous silica. DFT ^{13}C NMR chemical shifts of the acid group and carboxylate in various models. Blue: carboxyl group, burgundy: methyl group.

ing the size of the basis set. It is however accurate enough to evaluate trends. None of the chemical shifts calculated for the π-coordinated species (137 ppm and 147 ppm) account for the signal at *ca.* 186.0 ppm, but there is a peak at *ca.* 142.8 ppm that can be attributed to these species or to THF degradation. Regarding σ-bonded species, the carbon deshielding is due to the σ-coordination on the metal surface, with the exception of the monodentate ethanoate shown in the left inset of Figure 6 (170 ppm). But it is not easy to distinguish a dimetallacycle ethanoate (δ: [177 - 186] ppm) from a σ-bonded ethanoic acid (δ: [180 - 185] ppm), on the contrary to the protons of the methyl group, which ^{1}H NMR chemical shifts were previously shown to be a good probe of the ethanoic acid *vs.* ethanoate presence at the surface. As an outcome of both the ^{1}H and ^{13}C NMR, experimental and calculated results, the ligands capping the NPs should be coordinated as ethanoates with a direct interaction of the oxygen atoms with the metal surface within a dimetallacycle.

Vibrational properties. To complete these surface state studies, and in order to confirm that the ligands are coordinated on the metal surface as ethanoates, an FT-IR analysis on a solid sample of purified $Ru_x(CH_3COOH)_{0.4y}$ NPs was performed in ATR mode using a spectrophotometer installed in a glove box. The experimental spectrum is reported in Figure 7 in comparison with the experimental one of sodium ethanoate [36–38] and calculated frequencies of the theoretical Ru-H, and Ru-ethanoate normal modes of vibration of the $2^{COO,H}$ model. The vibrational frequencies of the metal core were calculated as well and it is interesting to notice that no imaginary frequency was found. In other words, the chosen hcp shape of the metal core is still a thermodynamic minimum under such high coverage. Although $2^{COO,H}$ does not rigorously account for the experimental NPs, it is a relevant model for the purpose of the experimental peaks assignment, very close to

be an optimal surface composition (*vide infra*), with co-adsorbed H and CH_3COO^- species. We shall see now that a normal modes analysis together with sodium ethanoate data provide a clear assignment of most of the peaks.

The bands experimentally observed at 2970 cm^{-1} are attributed to the ν_{as} and ν_s vibration modes of the methyl group (-CH$_3$) of the carboxylic moiety. Their theoretical counterpart are slightly overestimated by $\sim$200 cm^{-1} with respect to experimental data, as usual for C-H stretching modes within DFT calculations. [39] No carboxylic acid (-C=OOH) stretching vibration bands are visible in the region 1800-1600 cm^{-1}, indicating the absence of ethanoic acid for which a C=O vibration band is expected around 1706 cm^{-1} in standard conditions. [40] Whereas experimentally the three bands that lie between 1600 and 1300 cm^{-1} are well separated, the corresponding theoretical counterparts are situated in a narrower domain (1510 - 1300 cm^{-1}). They correspond to the successive excitation of the asymmetric stretching modes of the carboxylate group ($\nu_{as}(COO)$), of the methyl group deformation mode ($\delta_{as}(CH_3)$) strongly coupled with the COO symmetric stretching mode ($\nu_s(COO)$), and of the symmetric deformation mode of Me ($\delta_s(CH_3)$), in agreement with former IR results obtained on sodium ethanoate. [36–38] The frequency of the $\nu_{as}(CO_2)$ mode is underestimated in our calculation (1510-1455 cm^{-1}, exp.: 1550 cm^{-1}), as a possible result of an overestimation of the Ru to COO back-donation. The five characteristic peaks of ethanoate that follow $\delta_s(CH_3)$ are well-separated. They successively correspond to $\rho(Me)$, $\nu(CC)$, $\delta_s(CO)$, $\omega(CO_2)$, $\rho(CO_2)$, and they are not shifted with respect to experiments (DFT domain *vs.* exp. $\bar{\nu}_{max}$: $\sim$1020-1000/1021, $\sim$930-920/939, $\sim$650-635/674, $\sim$590/615 and $\sim$530-490/498 cm^{-1}).

Four experimental bands (a-d) observed at 1220, 1150, 850 and 800 cm^{-1} do not correspond to any calculated soft mode in $2^{COO,H}$. On the basis of their frequencies, some CH$_3$COOH modes
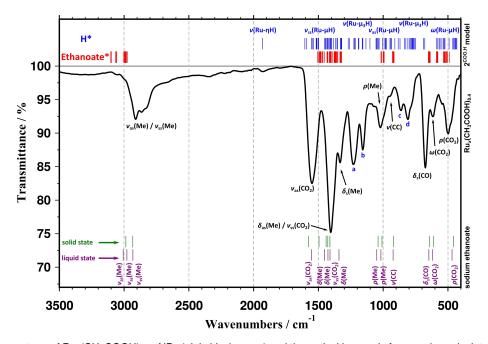
Fig. 7 Experimental IR spectrum of $Ru_x(CH_3COOH)_{0.4y}$ NPs (plain black curve) and theoretical harmonic frequencies calculated for $2^{COO,H}$ (Blue: Ru-H modes; red: Ru-CH$_3$COO modes) and assignment of the main peaks (regarding unassigned peaks, see the discussion in the text). The experimental peaks position and assignment of sodium ethanoate is also indicated: CH$_3$COONa in the solid state[36a] and in solution[36b,c]. ν_{ss}, ν_{as}: symmetric and asymmetric stretching; ω: wagging; ρ: rocking; δ: bending.

calculated in 2^{COOH} could account for three of these unassigned peaks, namely at 1243 cm^{-1}, δ_s(COH) at 1155 cm^{-1}, ν(CC) at 853 cm^{-1}. However, no peaks are observed experimentally around 1700 cm^{-1}, the domain that corresponds to ν(C=O), calculated to lie in 2^{COOH} at 1680 cm^{-1}, thus ruling out this first interpretation. Peaks a, c and d are rather attributed to the presence of silicon grease and of PFPE, a perfluoropolyether lubricant, that were used in the vacuum line and schlenk techniques to insure the inert atmosphere during the ruthenium NP synthesis.[41,42] Due to its presence during the purification process, THF could also be adsorbed on the surface, part of its IR signature being hidden below the ρ(Me) and c bands.[43,44] But it will be shown later on that its moderate adsorption energy on model **2** rules out this possibility. THF could also be indirectly responsible for the weak signal close to 1950 cm^{-1}, that may be attributed to a carbonyl group (CO) derived from THF degradation as previously observed with other ruthenium NPs (incidentally, Ru-H stretching modes are calculated to lie in the same domain frequency).[8] The last unassigned peak, b, could be attributed to polytetrahydrofuran (PTHF),[45] owing to a transitory adsorption of THF followed by ring-opening polymerization process. To conclude on this part, the results point out that the ligands surrounding the ruthenium NPs are not under the carboxylic acid form and confirm the deprotonation of the ethanoic acid upon coordination, now observed as a carboxylate by IR, as precedently by NMR.

2.4 Surface composition

Experimental titration of surface hydrides. Owing to the synthesis conditions (H$_2$ atmosphere), the presence of hydrides at the surface of the $Ru_x(CH_3COOH)_{0.4y}$ NPs was expected, as previously observed for other ruthenium NPs systems prepared in

the same manner.[7] The titration of surface hydrides was performed by investigating the particles as catalysts in the hydrogenation model reaction of norbornene at r.t. with no extra hydrogen added. The 2-norbornene conversion in the presence of $Ru_x(CH_3COOH)_{0.4y}$ NPs was observed to be low, but enough for its detection and quantification by GC analysis. The quantification of alkane formed by GC allowed determining the quantity of hydrogen atoms used for reducing the alkene, and further to calculate the H/surface Ru atomic ratio considering the nanoparticles mean size determined by TEM (1.5 nm). An estimated value of *ca.* 0.3 reactive hydrides per ruthenium surface atom (0.3 H$_{reac}$/Ru$_{surf}$) was found. This value appears a bit low compared to values previously determined for other ligand-stabilized ruthenium NPs that were in the range 1.0 - 1.6 H$_{reac}$/Ru$_{surf}$.[9,46] This result supports a difference in terms of surface state of the particles with less hydrides present.

Ru$_{55}$ DFT titration of surface species. It is possible to calculate the Gibbs free energy and other thermodynamic functions of solids and liquids, using first principles methods. Such approach has successfully been applied to explain or predict thermodynamic properties of materials, and in particular surface properties at the solid-gas interface.[47–50] In practice, it extends the $T = $ 0K and $p = $ 0Pa *ab initio* energies of surfaces covered by organic molecules coming from the surrounding medium to realistic environmental conditions in terms of temperature, pressure and composition of the gas and liquid surrounding phases, which is considered as a reservoir of species in equilibrium with the surface. These past years, it has been successfully applied to ruthenium surfaces and NPs, in equilibrium with molecular hydrogen only or with syngas.[31,33,51,52] The robustness and predictability of this approach is now going to be evaluated on the co-adsorption of
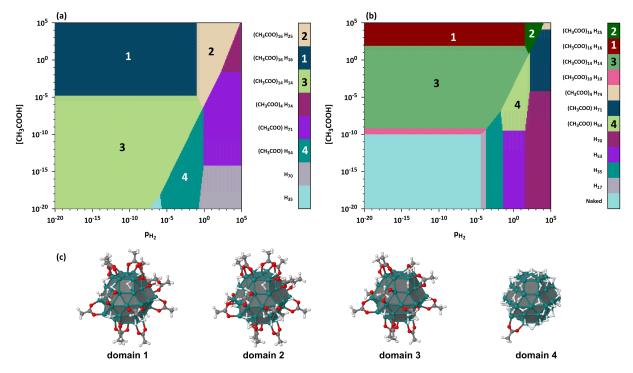
Fig. 8 $\Delta_a G^\circ(p_{H_2}, [CH_3COOH])$ phase diagram for H_2(gas) and CH_3COOH(liq) adsorption on Ru_{55} at (a) 300 K and (b) 450 K (pressure in bar, concentration in mol.L^{-1}). (c) Most stable [Ru_{55}] clusters in each domain 1-4 (domain 1: $Ru_{55}(CH_3COO)_{16}H_{16}$; domain 2: $Ru_{55}(CH_3COO)_{16}H_{25}$; domain 3: $Ru_{55}(CH_3COO)_{14}H_{14}$; domain 4: $Ru_{55}(CH_3COO)H_{54}$).

H_2 and CH_3COOH on model 1 (Ru_{55}). The 44 coverage possibilities that have been considered are summarized in the Methods section and listed in Table SI.9. Owing to the previous analysis of the spectroscopic data (IR and NMR), to the higher stability of adsorbed ethanoates with respect to adsorbed ethanoic acids, and to the very low COO-H activation barrier, 41 of these 44 structures exhibit no ethanoic acids on the metal surface.

Figure 8 shows two Gibbs free energies $\Delta_a G^\circ(p_{H_2}, [CH_3COOH])$ phase diagrams, calculated at $T = 300$ K and $T = 450$ K, which result from the DFT energies of the 44 structures, taking into account the ligand-metal vibration corrections (see Refs. 47 and 52). Note that the very low pressure and concentration domains are only plotted to show the appropriate relative positions of the stability domains with respect to higher pressure and concentration ones. Moreover the thermodynamic model is based on chemical potentials calculated for an ideal gas (H_2) or for an ideal mixture, thus making questionable the results shown for the very high pressure or concentration domains, but it nevertheless gives useful trends.

At r.t. (Fig. 8a), two stable surface compositions are found when p_{H_2} and [CH_3COOH] are in the range 10^{-20}-10^2 bar and 10^{-5}-10^5 mol.L^{-1}, respectively. For $p_{H_2} \lesssim 10^{-1}$ bar , the most stable species exhibits 16 ethanoates and 16 hydrides that can be seen as originating from the ethanoic acid deprotonation (($CH_3COO)_{16}H_{16}$, domain 1 in Fig. 8). Above this threshold, the ruthenium NP surface can accommodate 9 additional hydrides, thus resulting in an average 0.6 coverage value for H per Ru surface atoms ($Ru_{55}(CH_3COO)_{16}H_{25}$, domain 2). Note that the **2^{COO,H}** model ($Ru_{55}(CH_3COO)_{16}H_{33}$, structure 41 in Table SI.9) is very close to this surface composition.

Four stable surface compositions are found at 450 K within the same pressure and concentration domains previously considered at r.t (Fig. 8b). The $Ru_{55}(CH_3COO)_{16}H_{16}$ and $Ru_{55}(CH_3COO)_{16}H_{25}$ compounds are not any more the most stable structures around the acid concentration and hydrogen pressure of the experiments achieved in this study. The temperature increase requires a significant increase of the amount of acid and hydrogen in the surrounding medium in order to get such surface compositions. It is now $Ru_{55}(CH_3COO)_{14}H_{14}$ (domain 3) that is stable in the range 10^{-9}-10^2 mol.L^{-1} and with p_{H_2} below 10^{-1} to 10^2 bar according to the acid concentration. Although the dissociative adsorption energy of H_2 is low compared to that ofCH_3COOH, there is a competition between the desorption of hydrides and of ethanoic acids with respect to what is found at 300 K. Indeed, it is worth noting that there is a remarkable reversal of the H/ethanoate stoichiometry for a low acid concentration and a significantly high pressure of hydrogen, with a stable $Ru_{55}(CH_3COO)H_{54}$ structure (domain 4). This can be explained in terms of the metal surface energy, which relies upon the adsorption strength of each ligand and on the total number of ligands that are bound on a given metal surface area (parameter A in eq. 4, Methods section). It turns out that on a crowded metal surface the dissociative adsorption energy of a single ethanoic acid is $\sim$ -30 kcal.mol^{-1}, *i.e.* it is not significantly higher than the dissociative adsorption energy of H_2 ($\sim$ -22 kcal.mol^{-1}, see Ref. 33). Yet, owing to obvious steric considerations, a given surface area cannot accommodate as many ethanoate ligands as hydrides. The balance between similar adsorption energies, steric hindrance, zero-point energies of light ligands, pressure/concentration and temperature explains this drastic change in the surface composi-

tion on going from domain 3 to domain 4 in Figure 8.

Hydrides titration indicated that the ruthenim NP surface is covered by 0.3 H_{reac}/Ru_{surf}, meaning that at least around 13 H are adsorbed on the surface of the Ru_{55} NP model. DOSY NMR studies showed that at least 45% of the observed ligands are strongly bonded to the surface, the remaining ones being characterized by a fast diffusion coefficient. Ethanoates which have a strong interaction are the only one described in our theoretical structural model. This ratio suggests that at least *ca.* 12 carboxylates should be strongly bonded based on our NP model. Our theoretical model provides a quantity of species surrounding the NP a bit overestimated but presents the same trend as experimental data (high quantity of ligands and low amount of hydrides). Both theoretical studies and experimental findings are thus in a good agreement about the NP surface composition.
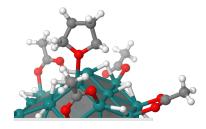

Fig. 9 Optimized geometry of $Ru_{55}H_{32}(CH_3COO)_{15}(THF)$.

On the possible presence of THF on the surface. $Ru_x(CH_3COOH)_{0.4y}$ NPs here studied were washed with THF prior to spectroscopic studies, THF was also used as a deuterated solvent for liquid NMR experiments. This opens the possibility for some THF molecules to adsorb on ruthenium NPs. In order to evaluate the possible competition with acid species on the metal surface, let us first compare the adsorption energy of THF and ethanoic acid on the $Ru_{55}(CH_3COO)_{15}H_{32}$ model (model **2**). The adsorption energy of the ethanoic acid was found to be -14.0 kcal.mol^{-1} (compound **2^{COOH}**), with an easy O-H dissociation that leads to an ethanoate and an hydride more stable than the adsorbed ethanoic acid by 15.9 kcal.mol^{-1} (compound **2^{COO,H}**). The η^1 grafting of THF on the metal surface of $Ru_{55}(CH_3COO)_{15}H_{32}$, which involves the σ-donation of one oxygen lone pair to a metal atom (Figure 9), is stable by -12.7 kcal.mol^{-1}. It can be inferred from these energies that the equilibrium exchange reaction **2^{COO,H}** + THF $\longleftrightarrow$ $Ru_{55}(CH_3COO)_{15}H_{32}(THF)$ + CH_3COOH is in favor of **2^{COO,H}**, the reaction being significantly endothermic by 17.2 kcal.mol^{-1}. As already commented on for the adsorption energy of the ethanoic acid or of the ethanoate, the THF/CH_3COOH exchange equilibrium depends on the total amount of adsorbed species. For example, the reaction $Ru_{55}(CH_3COO)_{14}H_{14}$ + THF $\longleftrightarrow$ $Ru_{55}(CH_3COO)_{13}H_{13}(THF)$ + CH_3COOH is endothermic by ~43 kcal.mol^{-1}. In conclusion, these results are not in favor of the presence of THF at the surface of ruthenium NPs.
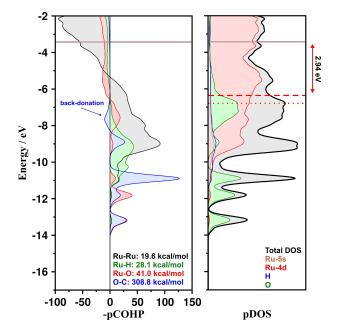
2.5 Electronic properties

Fig. 10 Projected DOS and COHP profiles for $Ru_{55}H_{33}(CH_3COO)_{16}$ (**2^{COO,H}**). Dashed red line and dotted red line on the pDOS profile: d-band center ($\bar{\varepsilon}_d$) of the 44 surface Ru atoms and of the 11 core Ru atoms, respectively; brown horizontal line: Fermi energy. The energies reported on the pCOHP graph are the IpCOHP indexes (see definition and references in the methods section).

Electronic states. The electronic structure of **2^{COO,H}** is now going to be compared with that of the bare Ru_{55} NP, which density of states and orbital-like analysis have already been published elsewhere.[33,53] Thanks to the Lobster software, the PAW electronic states were projected on a local Slater atomic basis set, hence giving the possibility to derive several properties and indexes, such as projected density of states (pDOS), crystal orbital hamilton population (pCOHP), bond strength indexes (IpCOHP) - see definitions and references in the Methods section. The d-band center[32,54] for the 44 surface metal atoms of the bare ruthenium NP was found to lie 2.6 eV below the Fermi energy, whereas the electronic structure of the 11 core atoms is more stable, with $\bar{\varepsilon}_d$ = 3.6 eV. As can be seen on the projected density of states (pDOS) plotted in Figure 10, the 33 hydrides and the 16 CH_3COO ligands stabilize the d-band center of surface atoms, which now lies at 2.94 eV, whereas core atoms are characterized by $\bar{\varepsilon}_d$ = 3.34 eV. The grafting of species on the metal surface also involves a weakening of the Ru-Ru bond strength, with the IpCOHP index per Ru-Ru bond equals to 19.6 kcal.mol^{-1} instead of 27.0 kcal.mol^{-1} in the bare Ru_{55} NP. In other words, the coordination of surface ligands leads to NPs of increased stability but involves a lowering by *ca.* 30% of the cohesive energy of the metal part of the NPs. As already found in our previous study about the co-adsorption of H and CO on ruthenium NPs,[33] the highest occupied states are essentially developed upon metal atoms, and they exhibit an anti-bonding character (negative -pCOHP). It is worth mentioning that some electrons populate anti-bonding C-O states (blue pCOHP curve in Figure 10) that lie at the same energy as bonding Ru-C states (red pCOHP curve in Figure 10). It can be analyzed as a weak back-donation from the metal surface to the π^* MOs of

the carboxylate groups. This is also in line with the average C-O bond length calculated to be 0.02 Å larger than in ethanoate at the DFT-PBE level of theory.

Are ethanoate-coated ruthenium NPs oxidized? The evolution of atomic charges upon the coordination is also of interest: do the grafted carboxylates change the oxidation state of surface ruthenium atoms? To answer this question, Bader charges as well as the Mulliken population analysis obtained by integrating the pDOS (pMPA charges) were calculated. In the $2^{\mathbf{COO,H}}$ case, the average atomic charge of the hydrides (Bader *vs.* pMPA: q_{Hy} = -0.19e/-0.20e), the global charges hold by functional groups (Bader *vs.* pMPA: q_{Me} = 0.14e/0.07e, q_{COO} = -0.67e/-0.55e) as well as the overall charge of the Ru$_{55}$ metal part (Bader *vs.* pMPA: q_{Ru} = 0.27e/0.26e) are found to be similar with both methods. The main differences lie in the atomic charges of the hydrogen atoms of the methyl group and of the main group elements (Bader *vs.* pMPA: $q_{C_{COO}}$ = 1.52e/0.64e, q_O = -1.10e/-0.59e, $q_{H_{Me}}$ = 0.07e/0.33e, $q_{C_{Me}}$ = -0.07e/-0.91e) as well as in the average charge hold by the 11 core metal atoms (Bader *vs.* pMPA: q_{Ru_c} = 0.04e/-0.12e). Whereas the two methods agree in concluding that surface Ru atoms are significantly oxidized (Bader *vs.* pMPA: q_{Ru_s} = 0.33e/0.35e - we will not introduce here a debate on the partial *vs.* formal atomic charges, but 1/3e is significantly positive), they differ about the charges on the 11 core metal atoms. According to the Bader analysis they are almost neutral whereas they are slightly negatively charged according to pMPA. In summary, the most striking difference between Bader and pMPA charges is observed for the core metal atoms and for the main group elements, with a possible overestimation by the Bader analysis of the charge difference between carbon and oxygen atoms.
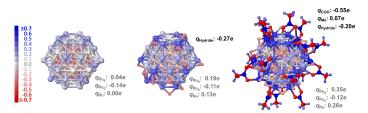

Fig. 11 Atomic pMPA charges in Ru$_{55}$, Ru$_{55}$H$_{17}$ and $2^{\mathbf{COO,H}}$ (from left to right), shown as color maps. The charge scale is shown on the left. Some selected partial charges are also shown (metal charges per Ru atom, q_{Ru}, or per core Ru atom, q_{Ru_c}, or per surface Ru atom, q_{Ru_s}).

There is of course no best partitioning of the electron charge density for all purposes.[55,56] It turns out that we recently observed for non-covalent doped graphene that pMPA charges are very similar to Natural Population Analysis charges.[57] Given also that pMPA charges are consistent with the pCOHP data and other values obtained from this projection scheme, such as the d-band center $\bar{\varepsilon}_d$, from now on they will be preferred. The pMPA charges of the Ru$_{55}$ NP, of the moderately hydrogenated Ru$_{55}$H$_{17}$ NP and of $2^{\mathbf{COO,H}}$ are graphically compared in Figure 11. Surface Ru atoms in Ru$_{55}$ are neutral or slightly positive (average charge q_{Ru_s}: 0.04e), whereas in Ru$_{55}$H$_{17}$ the hydrides hold a negative charge, thus involving a small oxidation of the surface Ru atoms

they are bound to (average charge q_{Ru_s}: 0.19e). The dissociative grafting of 16 CH$_3$COOH acids (compound $2^{\mathbf{COO,H}}$) involves a stronger oxidation of the surface Ru atoms, with a 0.35e average charge of the surface. Ru atoms on which carboxylates are grafted are even more oxidized, with charges that reach *ca.* 0.5e. It is interesting to compare these data with the charges calculated for Ru$_{55}$(CO)$_{66}$, another saturated Ru nanocluster previously studied by us.[33] It exhibits a weaker oxidation of surface Ru atoms, with an average charge q_{Ru_s} = 0.25e. It is not in contradiction with a low π-acceptor character of CO when coordinated to Ru surfaces[33] and it underlines the ability of ethanoate and hydrides to deplete the electronic density of surface Ru atoms. It is also worth mentioning that according to the charge calculations, all adsorbed hydrogen atoms in ethanoate-capped ruthenium NPs have an hydridic character, even those that originate from the acids.

3 What about the hydrogen evolution reaction as possible application?

As mentioned in the introduction, metal NPs can be used for several applications, ranging from catalysis to energy. Organometallic ruthenium NPs from the group have already been applied as catalysts mainly for hydrogenation reactions[7,9] and also more recently in hydrogen evolution reaction.[58] Considering the present study where we used carboxylates as new capping species on ruthenium NPs, the question of the interest of such NPs for HER application in the electrolysis of water can arise. This point is going to be now treated from the theoretical point of view. According to the seminal work of Nørskov,[17] there is a correlation between the H$_2$ dissociative adsorption Gibbs free energy ($\Delta G_{H^*} = \frac{1}{n}\left[G(nH^*) - G(\mathrm{surf}) - \frac{n}{2}G(H_2)\right]$) and the exchange current i_0 for HER. A Balandin-Sabatier volcano curve had been found, with platinum electrodes on top of the volcano and ΔG_{H^*} that lies between -2.0 kcal.mol^{-1} and +0.7 kcal.mol^{-1} as a function of H coverage. The main conclusion of this study is that the requirement for an optimal HER catalyst is that the Gibbs dissociative adsorption energy of H$_2$ must lie as close as possible to 0 kcal.mol^{-1}.

Although Pt-based catalysts show a high efficiency for reducing protons to H$_2$ in acidic media, there is a need to find alternative HER catalysts owing to the prohibitive cost of platinum. Ruthenium can be considered as an interesting candidate: it is approximately one order of magnitude cheaper than Pt, and it is close to fulfill the H adsorption Gibbs free energy criterion ($\Delta G_{H^*} \sim$ -7.9 and -2.6 kcal.mol^{-1} on Ru(0001) for 0.25 and 1.25 ML; results deduced from Ref. 31 after the empirical addition of 5.5 kcal.mol^{-1} as the representative thermal energy for all metals, see Ref. 17). Yet, the counterpart of this weak adsorption energy is that hydrogen may be scarcely present at the surface of ruthenium NPs when co-adsorbed with stabilizers that have a strong affinity with Ru, as recently demonstrated for ruthenium NPs in equilibrium with syngas where CO ligands were shown to occupy all grafting sites.[33] On the contrary, carboxylic acid-capped ruthenium NPs are good candidates for the HER owing to the surface composition previously studied, that shows a co-existence of carboxylates

with *ca.* [0.4-0.6] H/Ru$_{surf}$ at r.t (Figure 8, domains 1 and 2).

The adsorption energy of H, ΔE_{H^*}, has been calculated on five representative sites of the bare Ru$_{55}$ NP, and compared to those calculated on Ru$_{55}$(CH$_3$COO)$_{16}$H$_{16}$ and Ru$_{55}$(CH$_3$COO)H$_{54}$ models (domains 1 and 4 in Figure 8). ΔG_{H^*} energies calculated with eq. 2 are reported in Figure 12, together with the atomic d-band centers shown as color maps.[53] The bare Ru$_{55}$ NP shows a too strong $|\Delta G_{H^*}|$, whatever the adsorption site (between -8.8 and -10.3 kcal.mol^{-1}). $|\Delta G_{H^*}|$ is in general smaller for Ru$_{55}$(CH$_3$COO)H$_{54}$, in line with a significantly more stable atomic d-band center in this nanoparticle w.r.t. Ru$_{55}$. But, according to the weak ΔG_{H^*} criterion, that does not make NPs with such surface composition interesting candidates for HER. The calculated H$_2$ dissociative adsorption Gibbs free energies in Ru$_{55}$(CH$_3$COO)$_{16}$H$_{16}$, the model in best agreement with the experimental characterization, are weaker than those calculated for Ru$_{55}$(CH$_3$COO)H$_{54}$ on the same active sites (*ca.* -2 kcal.mol^{-1}). The d-band center model cannot account for the difference between the two models, since the $\bar{\varepsilon}_d$ values are the same (-2.90 eV for surface atoms). The weaker H-adsorption strength calculated in Ru$_{55}$(CH$_3$COO)$_{16}$H$_{16}$ is probably due to a strong Coulomb repulsion between the adsorbed hydride and the surface ethanoates. Such low adsorption energies position this catalyst on top of the volcano defined by Nørskov and co-workers,[17] thus making this nanomaterial a promising catalyst for HER..
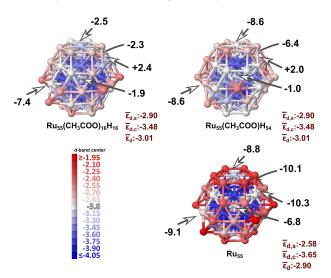

Fig. 12 d-band center color maps (scale in eV) for Ru$_{55}$, and for Ru$_{55}$(CH$_3$COO)$_{16}$H$_{16}$ and Ru$_{55}$(CH$_3$COO)H$_{54}$ (domains 1 and 4 in Figure 8). The dissociative adsorption Gibbs free energies of H$_2$, ΔG_{H^*}, are given in kcal.mol^{-1} (see text for details). The arrows indicate the probed adsorption sites. The surface, core and total average d-band center values are also given (in eV).

4 Conclusion

To summarize, in this study we report that ethanoic acid can be used as a stabilizing agent to prepare small ruthenium NPs and their full characterization at both experimental and theoretical level. On the basis of the combined data obtained, it is shown that ethanoic acid ligand lies on the surface of the nanoparticles as ethanoate. This result is in agreement with a small activation

barrier of O-H bond dissociation. Moreover, the ethanoate form observed does not preclude the adsorption of a significant amount of hydrogen atoms at the NP surface, contrarily to strongly coordinated ligands, such as carbon monoxide. The optimal surface composition appears to be *ca.* [0.4 - 0.6] H/Ru$_{surf}$ and 0.4 ethanoates/Ru$_{surf}$. Better still, with such a composition the hydrogen adsorption energy is calculated to be only -2.0 to -3.0 kcal.mol^{-1}, which is an important pre-requisite for a material to be a good catalyst of the HER in the electrolysis of water. This will be the topic of a forthcoming study.

Methods

Synthesis of NPs and characterization techniques

Reagents. All operations for the synthesis of the CH$_3$COOH-stabilized ruthenium NPs were carried out using standard Schlenk tubes, Fisher–Porter bottle techniques or in a glove-box (MBraun) under argon atmosphere (Air Liquide, classe 2, U 1006). The solvents (tetrahydrofurane, THF; *n*-pentane) were purchased from Carlo-Erba, purified by filtration on adequate columns in a purification apparatus (MBraun) and degassed according to a freeze–pump–thaw process just before use. The ruthenium precursor, [Ru(COD)(COT)] (Ruthenium-1,5-cyclooctadiene-1,3,5-cyclooctatriene), was synthesized from RuCl$_3$·xH$_2$O (Janssen) following an established procedure.[59] Glacial ethanoic acid 99.8% (CH$_3$COOH) was purchased from Acros Organics and degassed before use by bubbling argon for 30 min. Hydrogen gas was bought from Air Liquide (Alphagaz). THF-*d*^{8} for NMR studies were purchased from SDS and stored on activated molecular sieve into the glove box. Silica gel (pore size 60 Å) was gathered from Fluka Analytical, dried by thermal treatment (590 °C) under vacuum and then stored in the glovebox.

Synthesis of Ru$_x$(CH$_3$COOH)$_{0.2}$ and Ru$_x$(CH$_3$COOH)$_{0.4y}$ NPs. As a general procedure, Ru(COD)(COT) (30.0 mg; 0.095 mmol) was dissolved under argon in 20 mL of *n*-pentane in a Fisher Porter reactor. Then, the ethanoic acid, stabilizer, was added to the pale yellow Ru(COD)(COT) solution. Two different quantities of ethanoic acid compared to the Ru(COD)(COT) introduced were used, namely: 0.2 molar equivalent (1.14 mg; 0.019 mmol; Ru$_x$(CH$_3$COOH)$_{0.2}$) and 0.4 equiv. (2.29 mg; 0.038 mmol; Ru$_x$(CH$_3$COOH)$_{0.4y}$). After addition of the stabilizer, the reactor was pressurized with 3 bar of hydrogen (H$_2$) at room temperature and the initial yellow solution turned black in a few minutes. A vigorous magnetic stirring and the H$_2$ pressure were maintained for 30 min at r.t.. The synthesis carried out in the presence of 0.2 equiv. of ethanoic acid led to the formation of a precipitate in *ca.* 15 min under H$_2$ atmosphere while the reaction performed with 0.40 equiv. led to a colloidal suspension which remained stable in the same conditions. After 30 min, the H$_2$ pressure was evacuated and the reaction mixtures were concentrated under vacuum for TEM/HRTEM analysis.

Isolation and purification of Ru$_x$(CH$_3$COOH)$_{0.4y}$ NPs. The colloidal suspension of Ru$_x$(CH$_3$COOH)$_{0.4y}$ NPs was left under vacuum for 12h in order to eliminate the pentane used as solvent and the cyclooctane released from the decomposition of the Ru precursor. By this way, a dark grey powder was obtained

that was further used for analysis by 1D and 2D liquid-^{1}H NMR spectroscopy after dispersion in deuterated THF. Additionally, the Ru$_x$(CH$_3$COOH)$_{0.4y}$ powder was washed with pentane and THF and dried again under vacuum to get a highly purified sample for characterization by WAXS, solid-state NMR and Infrared spectroscopy.

Quantification of surface Hydrides. The quantification of hydrides adsorbed onto the surface of the NPs was carried out by gas chromatography (GC) analysis on a THF colloidal suspension following a previously described procedure.[60] 10 equivalents of olefin (2-norbornene) were added to a colloidal suspension of the NPs and the reaction mixture was maintained at r.t. under vigourous stirring during 72 h. Samples were taken from the mixture for GC analysis and estimation of the norbornene conversion into norbornane was done. The measurement of the amount of alkane formed by GC analysis (see below the analysis details) allowed to determine the necessary quantity of hydrogen atoms for reducing the alkene, and further to calculate the H$_{reac}$/Ru$_{surf}$ ratio considering the nanoparticle mean size obtained by TEM.

The quantity of surface metal atoms was obtained by following the next equations. $N = \left(\frac{NP_{diameter}}{2b(Ru_{radio})}\right)^3$ where N is the total number of Ru atoms per NP and b is the crystalline closed packed parameter.[61] $N = \frac{1}{3}\left(10n^3 - 15n^2 + 11n - 3\right)$ where n is the number of shells according to the magic number for metallic clusters. $N_{surf} = 10n^2 - 20n + 12$ where N_{surf} is the number of Ru surface atoms per NP.[62] The quantity of hydrides was calculated by the next equation $n_H = 2\left(n_{oleofin}\right)\left(\%_{Conv}\right)$ where $\%_{Conv}$ is the 2-norbornene hydrogenation percentage. The number of hydrides per Ru surface atom was obtained following the next relation $H_{reac}/Ru_{surf} = \left(\frac{n_H}{n_{Ru}}\right)\left(\frac{N_{surf}}{N}\right)$.

Transmission Electron Microscopy (TEM) and High Resolution TEM (HRTEM). Transmission electron microscopy analysis were performed at the "Centre de Microcaractérisation Raymond Castaing" in Toulouse (UMS-CNRS 3623). Samples were prepared by slow evaporation of a drop of the crude and concentrated colloidal suspension deposited onto a carbon-covered copper grid. TEM analysis were performed using a JEOL JEM 1011 microscope or a JEOL JEM 1400 one operating at 100 kV and 120 kV, respectively, and with a point resolution of 0.45 nm. HRTEM analysis was carried out using a JEOL JEM-ARM 200F microscope working at 200 kV with a point resolution of <0.19 nm. Size distributions were built by measuring ca. 400 nanoparticles through a manual counting of several enlarged TEM micrographs. The mean diameters of nanoparticles were determined by fitting a Gaussian curve to each statistical size distribution. FFT treatments of HRTEM images were carried out with Digital Micrograph Version 1.80.70 in order to determine the crystalline structure and the lattice parameter of the Ruthenium part of the NPs.

Wide-angle X-Ray scattering (WAXS). Measurements were performed at CEMES-CNRS in Toulouse. Samples were sealed in 1.0 mm diameter Lindemann glass capillaries. The samples were irradiated with graphite monochromatized molybdenum Kα (0.071069 nm) radiation and the X-ray scattering intensity mea-

surements were performed using a dedicated two-axis diffractometer. Radial distribution functions (RDF) were obtained after Fourier transformation of the corrected and reduced data.

Nuclear Magnetic Resonance (NMR) spectroscopy. Liquid proton NMR (1H-NMR) and diffusion-ordered spectroscopy (DOSY) experiments were performed on a Bruker Avance 500 spectrometer and on a Bruker Avance NEO 600 at 298 K. Preparation of the NMR tubes was carried out under argon atmosphere to avoid any oxidation of the NPs using deuterated tetrahydrofurane (THF-d^8) to disperse the nanoparticles powder. DOSY measurements were performed with a diffusion delay (Δ) of 90.0 ms and gradient pulse length (δ) of 2.0 ms. The peak integration decay curves of the DOSY spectra were fitted according to the Stejskal-Tanner function.[63] Solid-state NMR analysis were accomplished on a Bruker Avancelll 400WB spectrometer . Preparation of the sample was performed in a globe box to limit oxidation. The powder of Ru$_x$(CH$_3$COOH)$_{0.4y}$ NPs was diluted in mesoporous silica (60 Å) by impregnation (THF colloidal suspension) before filling a 3.2 mm rotor, followed by slow solvent evacuation. Experiments were conducted at a spinning speed of ca.12 KHz, using a ^{13}C spin-Echo and CPMG pulse sequence.

Calculation of Hydrodynamic radios. Hydrodynamic radios were estimated from the diffusion coefficients measured in 2D-DOSY experiments by following the Stokes-Einstein equation for spherical particles: $r = \frac{K_B T}{6\pi \eta D}$

Fourier Transform Infrared (FT-IR) spectroscopy. FT-IR spectra were recorded under inert atmosphere in a globe-box on a Perkin-Elmer GX2000 spectrometer in the Attenuated total reflection (ATR) mode and in the range 4000-400 cm^{-1}.

Gas Chromatography (GC). GC analyses were performed with a Hewlett Packard HP-5890 Series II instrument equipped with a flame ionization detector and a 30 m non polar capillary column (0.32 mm diameter, 0.25 mm film thickness) of dimethylpolysiloxane (SGE BP1), using helium (2 mL.min^{-1}) as a carrier gas; the temperature of the injector was set at 250 °C and that of the column at 60 °C (3 min). Each analysis was performed using a temperature set from 60 to 170 °C (15°C.min^{-1}).

DFT calculations

The Ru$_{55}$ model and other geometry features. It has previously been published and detailed elsewhere.[33] Briefly, it was shaped by slicing an hcp structure by two (001) planes and (101) planes. A tip has been added in order to introduce one B$_4$ and one B$_5$ site. Removing one line of atoms between two (101) planes generates a slightly corrugated facet. Such defects can probably be found on NPs larger than this ultra-small 1nm model. With 11 Ru atoms in the core, the surface area of the DFT-PBE optimized cluster is 258 Å^2. In order to define the bridging character μ_n and the hapticity η^m, we have considered an atom of the ad-ligand as coordinated to a given metal atom when the metal-atom distance is lower than 2.1 Å for H, 2.5 Å for C and 2.3 Å for O.

Sterically-driven distribution of ligands on the surface. Several of the 44 surface coverage possibilities considered in Section 2.4 were generated with our *dressNPs* home-made utility.[52] In

short, acids and hydrides were uniformly distributed on the surface by minimizing the steric hindrance between surface species with a Monte-Carlo simulated annealing algorithm. Other geometries with a low surface coverage were generated by randomly removing surface species from structures with a higher amount of ligands.

Periodic DFT calculations of metal nanoclusters. Software: Vienna *ab initio* simulation package, VASP.[64,65]; spin polarized DFT; exchange-correlation potential approximated by the generalized gradient approach proposed by Perdew, Burke, and Ernzerhof (PBE);[66] projector augmented waves (PAW) full-potential reconstruction;[67,68] PAW data sets for metal atoms treating the $(n-1)p$, $(n-1)d$ and ns states (*i.e.* 14 valence electrons for Ru); kinetic energy cutoff: 500 eV;[31,33,53] Γ-centered calculations;[69] Gaussian smearing of 0.02 eV width; geometry optimization threshold: residual forces on any direction less than 0.02 eV/Å; supercell size set to ensure a vacuum space of *ca.* 16 Å between periodic images of metal clusters (for example, 27.0×27.0×27.5 Å for Ru$_{55}$).

Calculation of coordination d-band centers. Coordination and averaged d-band centers[32,54] were calculated with our home-made *tools4vasp* suite of utilities,[52] which uses the DOS projected on a local basis set by the Lobster package (pDOS and pCOHP calculations, *vide infra*). The atomic d-band center of an atom α, $\bar{\varepsilon}_d(\alpha)$, is calculated as:

$$\bar{\varepsilon}_d(\alpha) = \frac{\left(\sum_m \int_{E_{\min}}^{E_F} \varepsilon n_{d_m}(\alpha,\varepsilon)d\varepsilon\right)}{\left(\sum_m \int_{E_{\min}}^{E_F} n_{d_m}(\alpha,\varepsilon)d\varepsilon\right)} \quad (1)$$

where m runs over the five d AOs and $n_{d_m}(\alpha,\varepsilon)$ is the atom-projected density of states on the d_m AO of atom α; μ_k is reminiscent of the symbol which designates bridging ligands in coordination chemistry and the bar sign above ε_d means that it is averaged over all d AOs; E_{min} is readily set to the bottom of the occupied d-band; DOS integrated up to the Fermi level E_F (see the discussion in ref.[53]); all calculated values are plotted as colored maps: hot spots for adsorption in red, blue for potentially weak interactions, white shows where intermediate adsorption processes should occur (white is defined by the electronic feature of the Ru(0001) slab).

HER. The free energy of the adsorbed state, H*, is calculated as

$$\Delta G_{H^*} = E(H^*) - E(\text{surf}) - \frac{1}{2}E(H_2) + \Delta E_{ZPE} - T\Delta S_H \quad (2)$$

In practice, N/orskov and co-workers have suggested that 5.5 kcal.mol^{-1} can be considered as representative of $\Delta E_{ZPE} - T\Delta S_H$ for all metals.[17] This means that $\Delta G_{H^*} = \Delta E_{H^*} + 5.5$ kcal.mol^{-1}. In some cases where the surface was very crowded, ΔE_{H^*} has been calculated by removing an hydrogen atom instead of grafting one, in order to avoid any spurious steric hindrance

pDOS, pCOHP and atomic charges calculations. pDOS and pCOHP profiles as well as bond energy analysis were achieved with the Lobster software, using the pbeVASPfit basis.[70–72] Ru: {4p, 4d, 5s, 5p}; H: {1s}; C, O: {ns, np}. At least $12n + m + 8k$ bands are calculated in VASP for a Ru$_{55}$H$_m$(X)$_k$ compound. The charge spilling, a criterion that assesses the quality of the projec-

tion, is systematically lower than 0.7%. Atomic charges are provided both by integrating the pDOS up to the Fermi energy and by carrying out the atoms-in-molecules (AIM) analysis of the charge density, proposed by R. W. F. Bader.[73] The former is nothing else than a Mulliken population analysis done with an orthogonal basis set, it has been called pMPA in the paper.

Qualitative average bond strength. This index can be obtained for a given A-B bond by integrating up to the Fermi energy the projected COHP values calculated between all valence μ and ν AOs that belong to A and B atoms, respectively:

$$\text{IpCOHP}(A-B) = \sum_{\mu \in A} \sum_{\nu \in B} \int_{E_{\min}}^{E_F} \text{pCOHP}_{\mu\nu}(\varepsilon)d\varepsilon \quad (3)$$

Such one-electron derived index must not be considered as a bond dissociation energy but it gives a valuable bond strength index which variation follows BDE variations or any property related to bond strength, such as A-B stretching frequencies.[33]

***ab initio* thermodynamics.** Let us consider a co-adsorption process of two species, L$_1$ and L$_2$, which is the starting point of the Langmuir-Hinshelwood mechanism in heterogeneous catalysis. It can be summarized as MNP $+ n_1L_1 + n_2L_2 = n_1L_1^* + n_2L_2^*$, and the Gibbs free energy for this reaction is calculated as:

$$\Delta_a G = [\Delta G° - n_1\mu(L_1, T, p) - n_2\mu(L_2, T, p)]/A \quad (4)$$

with:

$$\Delta G° = \Delta E + F^{\text{vib}}(n_1L_1^*) + F^{\text{vib}}(n_2L_2^*) \quad (5)$$

and A is the surface area of the metal core of the NP.

As the surrounding medium acts as a reservoir of ligands, the chemical potential for the ligand L can then be calculated from the standard chemical potential and the activity of the ligand:

$$\mu(L_i, T, p) = \mu^{\ominus}(L_i, T, p°) + kT \ln a(L_i) \quad (6)$$

$\mu^{\ominus}(L_i, T, p°)$ can usually be calculated from $H_T°$ and $S_T°$ values given in thermodynamic tables[74] ($\mu^{\ominus}(L_i, T, p°) = H_T°(L_i) - TS_T°(L_i)$) or computed from first-principles calculations done at 0K. In this case the standard chemical potential, *i.e.* $G_T°(L_i)$, is given by:[75]

$$\mu^{\ominus}(L_i, T, p°) = E^{\text{DFT}}(L_i) + H_T°(L_i) - TS_T°(L_i) \quad (7)$$

where $H_T°(L_i)$ and $S_T°(L_i)$ are usually calculated from the L partition function, *i.e.* by a straightforward application of the statistical thermodynamic equations.[75]

Surface adsorption Gibbs free energies $\Delta_a G$ can be plotted as a function of the two chemical potentials $\mu(L_1)$ and $\mu(L_2)$ for various surface compositions (n_1, n_2) and plausible thermodynamically stable geometries can then be highlighted on a surface phase diagram in the $[\mu(L_1), \mu(L_2)]$ space.

$H_T°(\text{EtAc}, g)$ and $S_T°(\text{EtAc}, g)$ were calculated with the Gaussian software, with THF taken into account as a solvent thanks to the SMD[76] variation of IEFPCM,[77,78] whereas $H_T°(H_2, g)$, $S_T°(H_2, g)$, were taken from the JANAF tables[74] (for example, $H_{298.15}°(H_2, g) = 8467$ J.mol^{-1}, $S_{298.15}°(H_2, g) = 130.68$ J.mol^{-1}.K^{-1},

$H^\circ_{298.15}(\text{EtAc}), g = 8671$ J.mol^{-1} and $S^\circ_{298.15}(\text{EtAc}), g = 197.65$ J.mol^{-1}.K^{-1}); the chemical potential for H is calculated as $\frac{1}{2}\mu(\text{H}_2, T, p)$, since it is the dissociative adsorption of H$_2$ that is considered. The surface area of the Ru$_{55}$ cluster was calculated by *dressNPs*, after identification of core and surface atoms ($A = 258$ Å^2). Free energy thermodynamic diagrams were produced with our home-made *aithermo* program.[52]

Reaction barriers. They were estimated by the climbing image nudge elastic band (CINEB) method[79–81] with a spring force between images of 5 eV and a force tolerance of 0.02 eV/Å. The harmonic vibrational modes were systematically calculated for in order to distinguish minima and saddle points by using the dynamical matrix code implemented in VASP as well as the VASPTST tools also developed in Henkelman's group.

NMR calculations on organic species on small metal clusters. Software: Gaussian09;[82] geometries fully optimized without any geometry constraints; PBE0 hybrid functional;[83] Chemical shielding tensors: Gauge Including Atomic Orbital (GIAO) method.[84–88]

Pseudopotentials and basis sets for [Ru$_6$] clusters are the same as in Ref.[23] (Basis set I). Relativistic effective core potentials developed by the Stuttgart group and their associated basis sets have been used for Ru[89] - augmented with an f polarization function (ζ_f: 1.577); H: 6-31G(d,p) basis set. C, O: Stuttgart ECPs and their associated basis set[90], with polarization functions (C : $\xi_d = 0.587$; O : $\xi_d = 0.961$).

Basis set for ethanoic acid and ethanoate: cc-pvtz (basis set II). Whereas ^{1}H and ^{13}C chemical shifts of ethanoic acid are found to be almost the same with basis set I and II, the basis set dependence is stronger with ethanoate.

TMS chemical shieldings. Polarized double-zeta basis set: $\sigma_\text{H} = 31.66$ ppm; $\sigma_\text{C} = 196.81$ ppm. cc-pvtz basis set: $\sigma_\text{H} = 31.57$ ppm; $\sigma_\text{C} = 189.16$ ppm.

Conflicts of interests

There are no conflicts of interest to declare.

Notes and references

1 *Nanoparticles and Catalysis*, ed. D. Astruc, Wiley-VCH, Weinheim (Germany), 2008.

2 J. Dupont and J. D. Scholten, *Chem. Soc. Rev.*, 2010, **39**, 1780.

3 *Nanoparticles. From theory to application*, ed. G. Schmid, Wiley-VCH, Weinheim, Germany, 2nd edn., 2010.

4 K. An, S. Alayoglu, T. Ewers and G. A. Somorjai, *J. Coll. Int. Sci.*, 2012, **373**, 1–13.

5 T. Sau and A. Rogach, *Complex-shaped Metal Nanoparticles: Bottom-Up Syntheses and Applications*, Wiley, Weinheim, Germany, 2012.

6 I. Favier, S. Massou, E. Teuma, K. Philippot, B. Chaudret and M. Gómez, *Chem. Comm.*, 2008, 3296.

7 K. Philippot, P. Lignier and B. Chaudret, in *Ruthenium in Catalysis*, ed. P. H. Dixneuf and C. Bruneau, Springer International Publishing, Switzerland, 2014, vol. 48 of Topics in Organometallic Chemistry, pp. 319–370.

8 L. M. Martínez-Prieto, C. Urbaneja, P. Palma, J. Cámpora, K. Philippot and B. Chaudret, *Chem. Comm.*, 2015, **51**, 4647–4650.

9 L. M. Martínez-Prieto and B. Chaudret, *Acc. Chem. Res.*, 2018, **51**, 376–384.

10 F. Leng, I. C. Gerber, P. Lecante, A. Bentaleb, A. Muñoz, B. M. Illescas, N. Martín, G. Melinte, O. Ersen, H. Martinez, M. R. Axet and P. Serp, *Chem. Eur. J.*, 2017, **23**, 13379–13386.

11 H. Fahrenfort, L. L. van Reyen and W. M. H. Sachtler, in *Mechanism of Heterogeneous Catalysis*, ed. J. H. de Boer, Elsevier, Amsterdam, 1960, ch. The decomposition of HCOOH on metal catalysts, pp. 23–48.

12 J. M. Thomas and W. J. Thomas, *Principles and Practice of Heterogeneous Catalysis*, Wiley-VCH, 2nd edn., 2015.

13 M. Grasemann and G. Laurenczy, *Energy Environ. Sci.*, 2012, **5**, 8171.

14 J. N. Brønsted, *Chem. Rev.*, 1928, **5**, 231–338.

15 H. Eyring and M. Polanyi, *Z. Phys. Chem. B-Chem. Elem. Aufbau. Mater.*, 1931, **12**, 279–311.

16 I. Chorkendorff and J. W. Niemantsverdriet, *Concepts Of Modern Catalysis And Kinetics*, Wiley-VCH, 2003.

17 J. K. Nørskov, T. Bligaard, A. Logadottir, J. R. Kitchin, J. G. Chen, S. Pandelov and U. Stimming, *J. Electrochem. Soc.*, 2005, **152**, J23–J26.

18 A. Roucoux, A. Nowicki and K. Philippot, in *Nanoparticles and Catalysis*, ed. D. Astruc, Wiley-VCH Verlag GmbH & Co. KGaA, 2008, pp. 349–388.

19 N. Liakakos, B. Cormary, X. Li, P. Lecante, M. Respaud, L. Maron, A. Falqui, A. Genovese, L. Vendier, S. KoÃ¯nis, B. Chaudret and K. Soulantica, *J. Am. Chem. Soc.*, 2012, **134**, 17922–17931.

20 P.-J. Debouttière, Y. Coppel, A. Denicourt-Nowicki, A. Roucoux, B. Chaudret and K. Philippot, *Eur. J. Inorg. Chem.*, 2012, **2012**, 1229–1236.

21 M. Guerrero, Y. Coppel, N. T. T. Chau, A. Roucoux, A. Denicourt-Nowicki, E. Monflier, H. Bricout, P. Lecante and K. Philippot, *ChemCatChem*, 2013, **5**, 3802–3811.

22 I. Favier, P. Lavedan, S. Massou, E. Teuma, K. Philippot, B. Chaudret and M. Gómez, *Top. Catal.*, 2013, **56**, 1253–1261.

23 I. del Rosal, F. Jolibois, L. Maron, K. Philippot, B. Chaudret and R. Poteau, *Dalton Trans.*, 2009, 2142–2156.

24 T. Gutmann, B. Walaszek, X. Yeping, M. Wächtler, I. del Rosal, A. Grünberg, R. Poteau, R. Axet, G. Lavigne, B. Chaudret, H.-H. Limbach and G. Buntkowsky, *J. Am. Chem. Soc.*, 2010, **132**, 11759–11767.

25 I. del Rosal, T. Gutmann, B. Walaszek, I. C. Gerber, B. Chaudret, H.-H. Limbach, G. Buntkowsky and R. Poteau, *Phys. Chem. Chem. Phys.*, 2011, **13**, 20199–20207.

26 T. Gutmann, I. del Rosal, B. Chaudret, R. Poteau, H.-H. Limbach and G. Buntkowsky, *ChemPhysChem*, 2013, **14**, 3026–3033.

27 L. M. Martínez-Prieto, I. Cano, A. Márquez, E. A. Baquero, S. Tricard, L. Cusinato, I. del Rosal, R. Poteau, Y. Coppel, K. Philippot, B. Chaudret, J. Cámpora, and P. W. N. M. van Leeuwen, *Chem. Sci.*, 2017, **8**, 2931–2941.

28 L. Foppa, K. Yamamoto, W.-C. Liao, A. Comas-Vives and C. Copéret, *J. Phys. Chem. Lett.*, 2018, 3348–3353.

29 H. E. Gottlieb, V. Kotlyar and A. Nudelman, *J. Org. Chem.*, 1997, **62**, 7512–7515.

30 J. A. Herron, J. Scaranto, P. Ferrin, S. Li and M. Mavrikakis, *ACS Catal.*, 2014, **4**, 4434–4445.

31 I. del Rosal, L. Truflandier, R. Poteau and I. C. Gerber, *J. Phys. Chem. C*, 2011, **115**, 2169–2178.

32 B. Hammer and J. K. Nørskov, *Surf. Sci.*, 1995, **343**, 211–220.

33 L. Cusinato, L. M. Martinez-Prieto, B. Chaudret, I. del Rosal and R. Poteau, *Nanoscale*, 2016, **8**, 10974–10992.

34 L. E. Marbella and J. E. Millstone, *Chem. Mater.*, 2015, **27**, 2721–2739.

35 P. Lara, O. Rivada-Wheelaghan, S. Conejero, R. Poteau, K. Philippot and B. Chaudret, *Angew. Chem., Int. ed. Eng.*, 2011, **50**, 12080–12084.

36 L. H. Jones and E. McLaren, *J. Chem. Phys.*, 1954, **22**, 1796–1800.

37 K. Ito and H. J. Bernstein, *Can. J. Chem.*, 1956, **34**, 170–178.

38 H. Noma, Y. Miwa, I. Yokoyama and K. Machida, *Journal of Molecular Structure*, 1991, **242**, 207–219.

39 C. Fábri, T. Szidarovszky, G. Magyarfalvi and G. Tarczay, *J. Phys. Chem. A*, 2011, **115**, 4640–4649.

40 J.-J. Max and C. Chapados, *J. Phys. Chem. A*, 2004, **108**, 3324–3337.

41 D. W. Mayo, F. A. Miller and R. W. Hannah, *Course notes on the interpretation of infrared and Raman spectra*, Wiley-Interscience, 2004.

42 H. C. Cui, D. C. Li and C. Wang, *Adv. Mat. Res.*, 2011, **391-392**, 1311–1314.

43 M. Zikmund and v. Štepničková, *Chem. Pap. - Chem. Zvesti*, 1969, **11-12**, 850–855.

44 A. L. Wayda, *Organometallics*, 1983, **2**, 565–566.

45 H. Deng, Z. Shen, L. Li, H. Yin and J. Chen, *J. Appl. Polym. Sci.*, 2014, **131**, 40503.

46 C. Amiens, D. Ciuculescu-Pradines and K. Philippot, *Coord. Chem. Rev.*, 2016, **308**, 409–432.

47 K. Reuter and M. Scheffler, *Phys. Rev. B*, 2001, **65**, 035406.

48 W.-X. Li, C. Stampfl and M. Scheffler, *Phys. Rev. B*, 2003, **68**, 165412.

49 C. Arrouvel, M. Digne, M. Breysse, H. Toulhoat and P. Raybaud, *J. Catal.*, 2004, **222**, 152–166.

50 K. Reuter, C. Stampfl and M. Scheffler, in *Handbook of Materials Modeling*, ed. S. Yip, Springer, Berlin, Heidelberg, 2005, vol. 1, ch. *ab initio* atomistic thermodynamics and statistical mechanics of surface properties and functions, pp. 149–194.

51 A. Comas-Vives, K. Furman, D. Gajan, M. C. Akatay, A. Lesge, F. Ribeiro and C. Copéret, *Phys. Chem. Chem. Phys.*, 2016, **18**, 1969–1979.

52 L. Cusinato, I. del Rosal and R. Poteau, *Dalton Trans.*, 2017, **46**, 378–395.

53 I. del Rosal, M. Mercy, I. C. Gerber and R. Poteau, *ACS Nano*, 2013, **7**, 9823–9835.

54 J. K. Nørskov, T. Bligaard, J. Rossmeisl and C. H. Christensen, *Nat. Chem.*, 2009, **1**, 37–46.

55 K. B. Wiberg and P. R. Rablen, *J. Comp. Chem.*, 1993, **14**, 1504–1518.

56 K. C. Gross, P. G. Seybold and C. M. Hadad, *Int. J. Quant. Chem.*, 2002, **90**, 445–458.

57 I. C. Gerber and R. Poteau, *Theo. Chem. Acc.*, 2018, 1.

58 S. Drouet, J. Creus, V. Collière, C. Amiens, J. García-Antón, X. Sala and K. Philippot, *Chem. Commun.*, 2017, **53**, 11713–11716.

59 P. Pertici, G. Vitulli, M. Paci and L. Porri, *J. Chem. Soc., Dalton Trans.*, 1980, 1961.

60 J. García-Antón, M. R. Axet, S. Jansat, K. Philippot, B. Chaudret, T. Pery, G. Buntkowsky and H.-H. Limbach, *Angew. Chem., Int. ed. Eng.*, 2008, **47**, 2074–2078.

61 H. Hosseini-Monfared, H. Meyer and C. Janiak, *J. Mol. Catal. A: Chem.*, 2013, **372**, 72–78.

62 B. K. Teo and N. J. A. Sloane, *Inorg. Chem.*, 1985, **24**, 4545–4558.

63 E. O. Stejskal and J. E. Tanner, *J. Chem. Phys.*, 1965, **42**, 288–292.

64 G. Kresse and J. Fürthmuller, *Phys. Rev. B*, 1996, **54**, 11169–11186.

65 G. Kresse and J. Fürthmuller, *Comput. Mater. Sci.*, 1996, **6**, 15–50.

66 J. P. Perdew, K. Burke and M. Ernzerhof, *Phys. Rev. Lett.*, 1996, **77**, 3865–3868.

67 P. Blöchl, *Phys. Rev. B*, 1994, **50**, 17953–17979.

68 G. Kresse and D. Joubert, *Phys. Rev. B*, 1999, **59**, 1758–1775.

69 H. J. Monkhorst and J. D. Pack, *Phys. Rev. B*, 1976, **13**, 5188–5192.

70 V. L. Deringer, A. L. Tchougréeff and R. Dronskowski, *J. Phys. Chem. A*, 2011, **115**, 5461–5466.

71 S. Maintz, V. L. Deringer, A. L. Tchougréeff and R. Dronskowski, *J. Comp. Chem.*, 2013, **34**, 2557–2567.

72 S. Maintz, V. L. Deringer, A. L. Tchougréeff and R. Dronskowski, *J. Comp. Chem.*, 2016, **37**, 1030–1035.

73 R. W. F. Bader, *Atoms in Molecules: A Quantum Theory*, Clarendon Press, Oxford University Press, New York, 1994.

74 M. W. Chase Jr., C. A. Davies, J. R. Downey Jr, D. J. Frurip, R. A. McDonald and A. N. Syverud, *JANAF Thermochemical Tables*, U.S. National Bureau of Standards, 3rd edn., 1985, vol. 14.

75 D. A. McQuarrie, *Statistical Mechanics*, University Science Books, Sausalito, California (USA), 2nd edn., 2000.

76 A. V. Marenich, C. J. Cramer and D. G. Truhlar, *J. Phys. Chem. B*, 2009, **113**, 6378–6396.

77 S. Miertuš, E. Scrocco and J. Tomasi, *Chem. Phys.*, 1981, **55**, 117–129.

78 J. Tomasi, *Theor. Chem. Acc.*, 2004, **112**, 184–203.

79 G. Henkelman, B. P. Uberuaga and H. Jonsson, *J. Chem. Phys.*, 2000, **113**, 9901–9904.

80 G. Henkelman and H. Jonsson, *J. Chem. Phys.*, 2000, **113**, 9978–9985.

81 D. Sheppard, R. Terrell and G. Henkelman, *J. Chem. Phys.*, 2008, **128**, 134106–1–10.

82 M. J. Frisch, G. W. Trucks, H. B. Schlegel, G. E. Scuseria, M. A. Robb, J. R. Cheeseman, G. Scalmani, V. Barone, B. Mennucci, G. A. Petersson, H. Nakatsuji, M. Caricato, X. Li, H. P. Hratchian, A. F. Izmaylov, J. Bloino, G. Zheng, J. L. Sonnenberg, M. Hada, M. Ehara, K. Toyota, R. Fukuda, J. Hasegawa, M. Ishida, T. Nakajima, Y. Honda, O. Kitao, H. Nakai, T. Vreven, J. A. Montgomery, Jr., J. E. Peralta, F. Ogliaro, M. Bearpark, J. J. Heyd, E. Brothers, K. N. Kudin, V. N. Staroverov, R. Kobayashi, J. Normand, K. Raghavachari, A. Rendell, J. C. Burant, S. S. Iyengar, J. Tomasi, M. Cossi, N. Rega, J. M. Millam, M. Klene, J. E. Knox, J. B. Cross, V. Bakken, C. Adamo, J. Jaramillo, R. Gomperts, R. E. Stratmann, O. Yazyev, A. J. Austin, R. Cammi, C. Pomelli, J. W. Ochterski, R. L. Martin, K. Morokuma, V. G. Zakrzewski, G. A. Voth, P. Salvador, J. J. Dannenberg, S. Dapprich, A. D. Daniels, O. Farkas., J. B. Foresman, J. V. Ortiz, J. Cioslowski and D. J. Fox, *Gaussian 09 Revision D.01*, Gaussian Inc. Wallingford CT 2009.

83 C. Adamo and V. Barone, *J. Chem. Phys.*, 1999, **110**, 6158–6170.

84 F. London, *J. Phys. Radium*, 1937, **8**, 397–409.

85 R. McWeeny, *Phys. Rev.*, 1962, **126**, 1028–1034.

86 R. Ditchfield, *Mol. Phys.*, 1974, **27**, 789–807.

87 J. L. Dodds, R. McWeeny and A. J. Sadlej, *Mol. Phys.*, 1977, **34**, 1779–1791.

88 K. Woliński, J. F. Hinton and P. Pulay, *J. Am. Chem. Soc.*, 1990, **112**, 8251–8260.

89 M. Dolg, U. Wedig, H. Stoll and H. Preuss, *J. Chem. Phys.*, 1987, **86**, 866–872.

90 A. Bergner, M. Dolg, W. Küchle, H. Stoll and H. Preuß, *Mol. Phys.*, 1993, **80**, 1431–1441.